Materials & Design 233 (2023) 112259

Contents lists available at ScienceDirect

Materials & Design

journal homepage: www.elsevier.com/locate/matdes

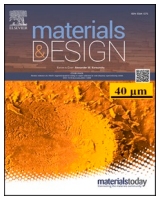

Constrained incipient phase transformation in Ni-Mn-Ga films: A small-scale design challenge

Adnan Fareed [a], Julian M. Rosalie [a], Sourabh Kumar [a], Satyakam Kar [b,c], Tilmann Hickel [a,d], Sebastian Fähler [b,c], Robert Maaß [a,e,*]

[a] Federal Institute of Materials Research and Testing (BAM), Unter den Eichen 87, 12205 Berlin, Germany
[b] Leibniz IFW Dresden, Institute for Metallic Materials, Helmholtzstr. 20, 01069 Dresden, Germany
[c] Helmholtz-Zentrum Dresden-Rossendorf, Bautzner Landstraße 400, 01328 Dresden, Germany
[d] Max-Planck-Institut für Eisenforschung GmbH, Düsseldorf D-40237, Germany
[e] Department of Materials Science and Engineering, University of Illinois at Urbana-Champaign, Urbana, IL 61801, USA

ARTICLE INFO

Keywords:
Shape-memory alloys
Nanoindentation
Incipient plasticity
NiMaGa

ABSTRACT

Ni-Mn-Ga shape-memory alloys are promising candidates for large strain actuation and magnetocaloric cooling devices. In view of potential small-scale applications, we probe here nanomechanically the stress-induced austenite–martensite transition in single crystalline austenitic thin films as a function of temperature. In 0.5 μm thin films, a marked incipient phase transformation to martensite is observed during nanoindentation, leaving behind pockets of residual martensite after unloading. These nanomechanical instabilities occur irrespective of deformation rate and temperature, are Weibull distributed, and reveal large spatial variations in transformation stress. In contrast, at a larger film thickness of 2 μm fully reversible transformations occur, and mechanical loading remains entirely smooth. Ab-initio simulations demonstrate how an in-plane constraint can considerably increase the martensitic transformation stress, explaining the thickness-dependent nanomechanical behavior. These findings for a shape-memory Heusler alloy give insights into how reduced dimensions and constraints can lead to unexpectedly large transformation stresses that need to be considered in small-scale actuation design.

1. Introduction

Metallic materials that can sustain reversible shape changes have found their way into numerous applications [1–4]. These include not only classical actuation devices that exploit reversible strains [5–7], but also potential cooling systems that rely on caloric effects [8,9]. Whilst traditional shape-memory alloys, such as NiTi [10,11], CuAlNi [12], or CuAlBe [13], offer significant phase-transformation induced strain-recovery upon thermal and/or mechanical stimuli, ferromagnetic shape-memory alloys provide further very large magnetic-field induced strains due to magnetically driven reorientations [14–16].

A particularly promising ferromagnetic shape-memory material is the Ni-Mn-Ga ternary system, in which $L2_1$ ordered compositions undergo a first-order phase transition between an austenitic high-temperature phase and a low temperature martensite phase [15–17]. Compositional variations and microstructural design allow tuning of the phase-transition temperature as well as the pseudoelastic switching strain, which can range between 6% and 24%, depending on the formed martensitic structure [16,18]. Indeed, different 10 M and 14 M modulated, as-well as non-modulated (NM) martensitic structures can be observed [17,19], and the occurrence of these structures can be explained by the so-called adaptive concept, which identifies the NM structure that exhibits the largest tetragonal distortion, as the ground state [20]. In addition, complex intermediate pre-martensitic structural arrangements have been reported, hinting towards a rather broad spectrum of metastable structures towards the formation of tetragonal martensite [21], and for which we recently revealed a hierarchical pre-martensitic microstructure [22].

Considering that the high-temperature austenite can admit substantial pseudoelastic strains upon mechanical actuation, any meaningful application relies on repeatedly undergoing a large number of reversible phase changes without functional fatigue. In other words, it becomes imperative to understand the point at which losses emerge due to structural damage that cause incomplete phase transformations and eventually functional fatigue. At the macroscopic scale, this is not straight-forward due to microplastic processes that are inaccessible to

* Corresponding author at: Federal Institute of Materials Research and Testing (BAM), Unter den Eichen 87, 12205 Berlin, Germany.
E-mail address: robert.maass@bam.de (R. Maaß).

https://doi.org/10.1016/j.matdes.2023.112259
Received 31 March 2023; Received in revised form 27 June 2023; Accepted 18 August 2023
Available online 19 August 2023

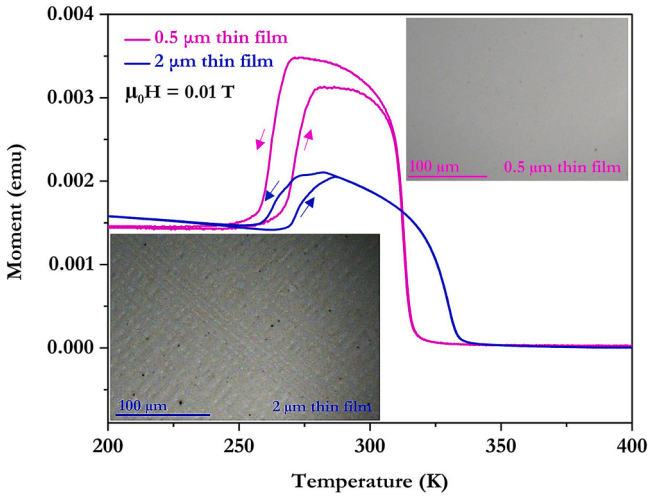

Fig. 1. Temperature dependent magnetization under a constant magnetic field of $\mu_0 H = 0.01$ T. The arrows indicate the heating–cooling sequence. The inset in the lower left corner visualizes via optical microscopy the martensitic microstructure below M_f during cooling of the 2 μm film, whereas the upper right inset shows a smooth surface above A_f during heating for 0.5 μm, indicative of the austenitic phase.

most bulk deformation experiments [23]. However, small-scale mechanical testing offers a sensitive alternative that not only can sample irreversible components of the underlying first-order transition, but in addition allows direct probing of the incipient phase transformation. For example, small-scale deformation of NiTi could reveal how pockets of residual martensite form within one deformation cycle, representing the onset of mechanical dissipation in a shape-memory alloy [24]. In contrast, the situation for Ni-Mn-Ga remains unclear both in terms of functional fatigue during cycling as well as in terms of incipient phase transformations upon loading. This is partly due to the fact that earlier nanomechanical work focused on as-prepared martensitic material [25], or due to high indentation loads used to study phase transformations via imaging after deformation [26,27]. Since a first-order transformation occurs, which also entails the co-existence of both phases, small-scale actuation may in fact begin at widely varying critical stresses. This in turn requires a statistical assessment at the small scale as opposed to the well-averaged bulk case. To this end, we conduct automated nanoindentation on Ni-Mn-Ga thin films, with a particular interest in assessing the onset of the martensitic phase transformation and possible residual martensite after deformation at small length scales.

To probe nano-scale deviations from purely elastic behavior and to shed light onto the incipient (pseudo)elastic or plastic response of Ni-Mn-Ga, we pursue here instrumented nanoindentation of single crystalline austenitic thin films as a function of temperature across the austenite–martensite transition temperature. Two film thicknesses of 0.5 μm and 2 μm were considered, both of which were austenitic at room temperature. We selected this state as a promising candidate for pseudoelastic and electrocaloric microsystems [28]. Nanoindentation reveals a marked plastic instability for the thinner film, with a Weibull distributed transformation stress in the range of 1.4–2.4 GPa that is independent of temperature and deformation rate. This is not the case for the larger film thickness that admits fully smooth loading behavior. Transmission electron microscopy reveals residual martensite at indentation sites of the thinner film, supporting the argument that the pop-in behavior stems from a stress-induced phase transition. In contrast, a fully reversible phase transformation must have occurred in the thicker film, since no structural changes were identified after loading. Ab-initio calculations are used to qualitatively rationalize the thickness-dependent incipient plastic behavior. These findings demonstrate how constraints can significantly increase the phase-transformation stress and contribute to irreversible processes during transformations, both of which must be taken into account in small-scale actuator design.

Table 1
Transition temperatures of phase transformations for both films. M_s is the temperature when martensite formation starts upon cooling from the austenite, and at M_f this transformation has finished. Correspondingly, A_s and A_f are the austenite start and finish temperatures during heating. The Curie temperature, T_c, is also given for both thin films.

Film thickness	M_s	M_f	A_s	A_f	T_C
0.5 μm	268 K	256 K	268 K	281 K	312 K
2 μm	274 K	257 K	270 K	285 K	332 K

2. Experimental and computational details

As described elsewhere [29], epitaxial Ni-Mn-Ga-films with thicknesses of 0.5 μm and 2 μm were prepared by DC Magnetron sputtering on single-crystal MgO (0 0 1) substrates with a 20 nm epitaxial Cr-buffer layer. The substrate temperatures during deposition were 600 °C and 400 °C for the thinner and thicker film, respectively. The sputtered thin films had compositions of $Ni_{54.5}Mn_{18.5}Ga_{27}$ (thinner film), and $Ni_{53.5}Mn_{20}Ga_{26.5}$ (thicker film), as determined by energy dispersive x-ray spectroscopy (EDX) with 1 at. % accuracy using a $Ni_{50}Mn_{25}Ga_{25}$ standard. Using a vibrating sample magnetometer (Quantum Design-VERSALAB) with a constant magnetic field ($\mu_0 H = 0.01$ T), the samples' phase-changing behavior was examined in the temperature range of 200 K to 400 K with a heating rate of 2 K/min. The magnetic field was applied along the MgO [1 0 0]-direction. Fig. 1 shows the resulting magnetization curves for both films, where arrows indicate the heating and cooling cycles and where the high temperature austenite phase shows an expected loss of the magnetic moment above the Curie temperature T_C.

Both films reveal minor composition-dependent differences in the austenitic start (A_s) and finish (A_f) temperatures, as well as in the martensitic start (M_s) and finish (M_f) temperatures. The values of these temperatures are summarized in Table 1 for the 0.5 μm and the 2 μm thin film. The insets in Fig. 1 display optical microscopy images that evidence the featureless austenite state expected above room temperature (upper right corner, 0.5 μm film) and the characteristic patterns of martensite variants below M_f (lower left corner, 2 μm film).

Temperature-dependent and rate-dependent nanoindentation was carried out using a Bruker-Hysitron TI980 instrument. For experiments conducted only at room temperature, a cono-spherical diamond tip with a radius of 890 nm was used. All experiments were done in load-controlled mode with a maximum load of 1 mN and at room temperature four different loading rates (1 mN/s, 0.1 mN/s, 0.01 mN/s, and 0.001 mN/s) were used. A holding time of 10 s at the maximum load was applied and all unloading segments had a loading rate of 0.1 mN/s. All indents were spaced 4 μm apart and at least 400 indents were done at each rate or temperature. The temperature-dependent nanoindentation experiments of both films followed the same testing protocol, but using the instruments Xsol-stage, another cono-spherical tip was necessary, which had a tip radius of 1 μm. A temperature range between 242 K and 313 K was covered, including both the martensitic phase at low temperatures and the austenite at higher temperatures (Fig. 1). For any temperature-dependent testing, the thin films were first placed inside its testing environment including thermocouples, heaters, and liquid nitrogen coolers, after which the sample was heated to 313 K. Stepwise cooling was followed to probe the nanomechanical response at lower temperatures. The sample environment was continuously purged with nitrogen gas to prevent water condensation on the sample surface.

Atomic force microscopy (AFM, MFP-3D Asylum instrument), a dual beam scanning-electron (SEM) and focus ion beam (FIB) microscope (Quanta 3D FEG from ThermoFischer) were used to map selected

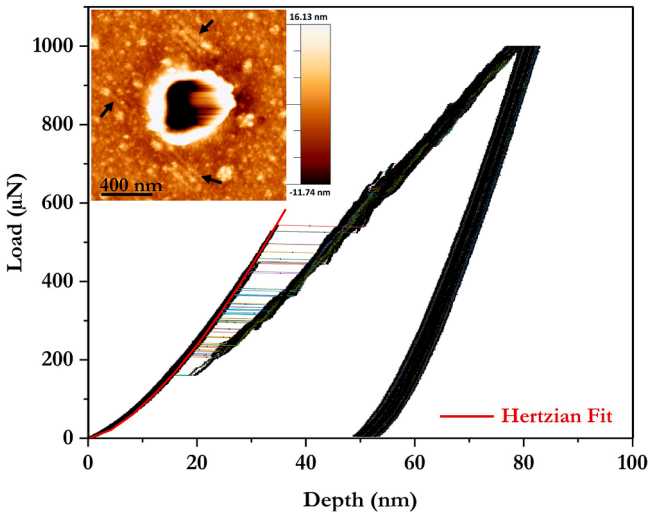

Fig. 2. A set of 70 load–displacement curves obtained at room temperature on the 0.5 μm thick film. Clear pop-in behavior is seen after an elastic loading segment that follows the Hertzian contact model. The inset displays an AFM image of an indent that is surrounded by line features marked by arrows that evidence residual martensite after deformation.

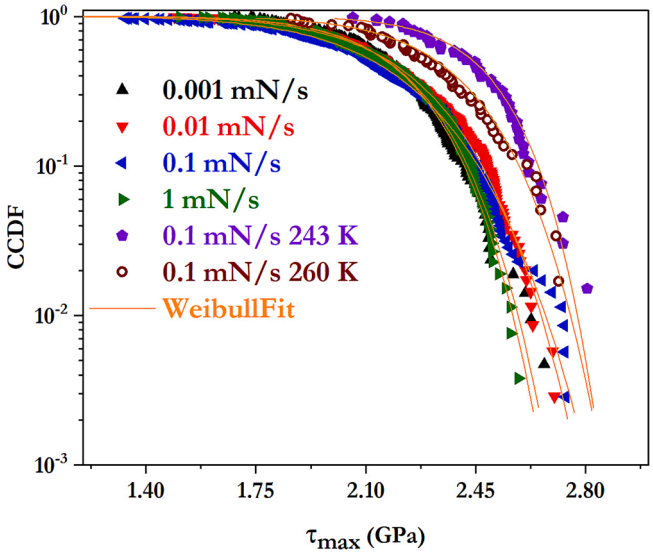

Fig. 3. A complementary cumulative distribution function (CCDF) of the first pop-in stress of the 0.5 μm thick film for different loading rates at room temperature and for at 0.1 mN/s at 243 K and 260 K. All data can be well described with a Weibull distribution. The corresponding fitting parameters are summarized in Table 2.

indentation sites prior and after nanomechanical testing. Transmission electron microscopy (TEM, JEM-2200FS) samples were extracted from indentation sites following standard FIB lift-out methods to investigate the microstructure underneath the indents.

Complementary to the experiment, ab-initio calculations were conducted. Specifically, spin-polarized density functional theory (DFT) calculations were performed with the Vienna ab initio simulation package (VASP) [30–33]. The plane-augmented wave (PAW) method [34,35] is used with GGA-PBE (Generalized gradient approximation as parametrized by Perdew-Burke-Ernzerhof) functionals [36] to describe the electron–ion interaction and exchange–correlation. A Γ-centered k point grid of 11 × 11 × 11 was used to sample the Brillouin zone. The energy and force convergence criteria were set to 10^{-8} eV and 0.01 eV/Å. A conjugate-gradient algorithm was used for relaxing and optimization of structural parameters. An energy cut-off of 500 eV was used for the representation of the Kohn-Sham wavefunction and truncation of plane-wave basis sets.

As indicated in the introduction, the martensitic transformation in the $Ni_{2+x}Mn_{1+y-x}Ga_{1-y}$ system is characterized by a change of the cubic unit cell to an orthorhombic one. Usually, the energy of the crystal structure as function of the c/a ratio is used to characterize the structural transformation. To evaluate the bulk thermodynamics, these calculations are often performed by keeping the volume fixed to the value of the austenite, since only small volumetric changes are observed in experiments across the transformation [37,38]. In order to consider the shape changes enforced by nanoindentation in the present manuscript, the assumption of constant volume is no longer justified. Instead, we are discussing a uniaxial compression along the c axis. For the in-plane lattice parameters, for which only the case $a = b$ is considered, different scenarios can be calculated: on the one hand, they can adapt to a value that minimizes the energy of the overall unit cell. As long as we describe a single phase, this will be determined by the Poisson ratio. On the other hand, they can be constrained by external boundary conditions, such as the lattice constant of the substrate onto which the thin films have been grown. Relying on these two scenarios, the potential energy for a range of different c/a and $a = b$ values for the stoichiometric Ni_2MnGa alloy was calculated and will be discussed in terms of the resulting potential energy surface (PES). At this stage, we note that the PES only captures the NM variant of the martensite, while experimentally observed martensite structures such as 10 M and 14 M are for simplicity not explicitly calculated. They are modulated variants of the NM martensite and due to the low energy of the involved twin-boundaries energetically similar to NM [20]. An important difference for the upcoming discussion is, however, that the modulated structures have an effective $c/a < 1$.

3. Results and discussion

3.1. Constraint-induced intermittent phase transformations

Nanoindentation on the 0.5 μm thin film at a rate of 0.1 mN/s reveals a clear plastic instability, also known as a pop-in that marks a deviation from the elastic contact. Fig. 2 displays a set of 70 nanoindentation curves on the 0.5 μm film together with the elastic solution of a Hertzian contact model, which was fitted according to $P = \frac{4}{3}E_r\sqrt{R}h^{3/2}$ [39], where P is the applied load, R is the indenter tip with radius of 890 nm, h is the penetration depth, and E_r (79 GPa) is the reduced modulus. Similar to indentation on single crystalline single element metallic materials, the first pop-in is significantly larger in displacement magnitude than any subsequent higher-order events [40–43]. Specifically, the first pop-in of the $Ni_{54.5}Mn_{18.5}Ga_{27}$ thin film typically exceeds 4 nm, whereas any higher-order instabilities are mostly 0.6–1.5 nm in size. In addition to a clear first pop-in signature, Fig. 2 also reveals a remarkable superposition of the continued loading curves after the first event. As such, the magnitude of the first pop-in scales with applied load, which is a feature known for a variety of metallic materials, including metallic glasses [44], superalloys [45], and intermetallics [46] that finds its origin in the stressed-volume indentation-depth scaling inherent to the experiment [47]. However, the rare occurrence and small size of additional pop-ins after the first, sets the data in Fig. 2 apart from dislocation plasticity or shear-localization and leads to indentation curves that fall well onto each other.

In case of the present shape-memory alloy, the clear pop-in signature after the elastic response could either originate from a stress-induced phase change from austenite to martensite or from plastic deformation involving dislocation activity. Whilst little data on incipient plastic behavior of shape-memory alloys exist, earlier work on NiTi has indeed revealed pop-ins [24]. In-situ SEM investigations at much higher loads (50 mN for a tip radius of 5 μm) and therefore displacements, suggested that the pop-in signature in NiTi originates from a phase transformation.

Table 2
Weibull shape parameter K and scale parameter λ across loading rates at room temperature and at 260 K for the corresponding distributions depicted in Fig. 3.

Loading rate (mN/s)	1	0.1	0.01	0.001	0.1 (260 K)
Shape parameter *K*	10.09	10.23	11.13	14.94	14.94
Scale parameter λ	0.47	0.49	0.48	0.48	0.39

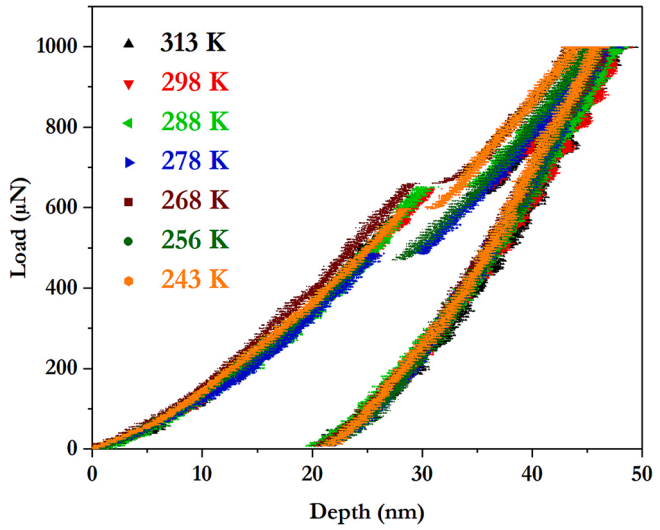

Fig. 4. Temperature dependent nanoindentation measurements done at 313 K to 243 K covering the fully austenite and martensite phase regime for the 0.5 μm thin film. Pop-ins are observed across all testing temperatures.

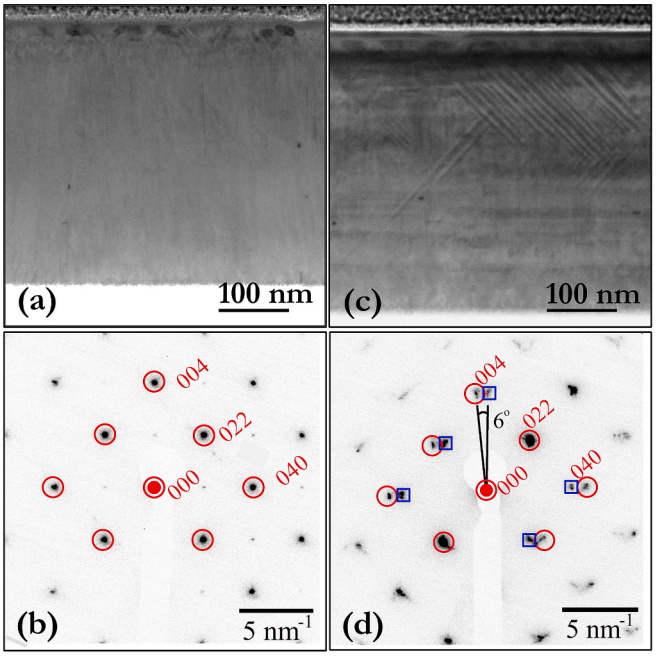

Fig. 5. (a) Bright field STEM image of the as-deposited austenite 0.5 μm thin film, revealing a pure single crystalline thin film. (b) the corresponding SAD pattern of image a), with beam direction $B = [100]$, demonstrating the austenitic film structure. (c) Bright field STEM image underneath one of the indents. The corresponding SAD pattern is shown in (d) revealing both austenite and residual martensite. Austenite and martensite reflections are indicated by circles and squares, respectively.

If this also holds for Ni-Mn-Ga, the large variation in the pop-in stress visible in Fig. 2 indicates a large statistical variation of the local phase transformation and its critical stress in epitaxial films, which is markedly different to a bulk single crystal.

To quantify this further, the pop-in force, P_p, ranging across all curves from ca. 100 to 600 μN, is converted to a shear stress via $\tau_{max} = 0.31\left(\frac{6P_pE_r^2}{\pi^3R^2}\right)^{1/3}$, using 79 GPa for E_r. This approach approximates the Poissons ratio of the tested material to 0.3 and is widely used for the statistical assessment of shear-stress statistics in metals [40,41]. Fig. 3 summarizes the obtained shear stresses using a complementary cumulative distribution function (CCDF). A CCDF, which is 1-CDF, where the latter is the cumulative distribution function, is preferred over the often-used probability density distribution (PDF), as it avoids binning and therefore reveals subtle but important properties of the distribution. Indeed, the CCDF emphasizes the lower-probability events and therefore highlights extreme stress-scale values of the probed mechanism. It is found that the room-temperature data is essentially distributed identically across all applied loading rates, with some deviations in the extreme value tail at low probabilities.

Subsequently, the maximum likelihood estimator (MLE) method [48] was used to quantitatively determine the appropriate distribution function for the pop-in stress data. This approach allows comparing various distribution models, being here a truncated power law, a log-normal distribution, and a stretched exponential (Weibull) distribution that are quantified via a log likelihood ratio (here between 1.4 and 2.9) and a significance value (here consistently smaller than 0.05) to evaluate which model is the best match to the actual data. All room-temperature data is best described by a Weibull distribution, of which the shape and the scale parameters are listed in Table 2. Identifying a Weibull distribution as the most suitable distribution for the pop-ins indicates a weakest-link scenario, which is often observed for strongly stress-driven microstructural mechanisms [49]. We therefore probe the statistics of the first critical stress for a given fluctuation in Fig. 3. This would be very much compatible with a diffusion less and often weakly rate-dependent transformation from austenite to tetragonal martensite.

Before we turn our attention to the microstructural change that admits the plastic instability, the pop-in response of the 0.5 μm film is also examined across the temperature range of the first order transition upon heating from the martensitic regime (Fig. 1). Fig. 4 displays typical indentation curves measured for temperatures between 313 K and 243 K.

In comparison to the room-temperature data, the noise level has increased from a standard deviation of 0.2 nm at 313 K to 0.6 nm at 243 K. This is expected due to the applied gas flow of the liquid nitrogen gas used for cooling. It is important to note that the low-temperature measurements were conducted with a larger tip radius, leading to reduced depth values at an identical maximum force in comparison to the before discussed room-temperature data. The lowest temperature in this series is probing a pure martensitic phase according to the magnetization curve (Fig. 1), but yet a very similar pop-in signature is present. Interestingly, the statistical signature of the pop-in at 243 K is also Weibull distributed, but significantly shifted to higher stress values than at room temperature (Fig. 3). This is not due to the marginally larger tip radius, which actually reduces the stress at otherwise identical load conditions. As such, the shifted CCDF is a clear indication for higher activation stresses for the underlying stress-relaxation mechanism that allows abrupt displacement increments. Given that the $Ni_{54.5}Mn_{18.5}Ga_{27}$ is in its martensitic state at 243 K, the change in stress scale must be linked to twin-variant reorientation [50] and twin-thickening [24] instead of originating from a austenite-to-martensite transition possible at higher temperatures. To further substantiate this conclusion, it is instructive to conduct a nanomechanical testing series at a temperature slightly higher than 243 K, such that one probes the material within the co-existence temperature of both martensite and austenite. When sampling the material at a number of random locations, one would thus expect a stress range of pop-ins at a given probability that now covers both the range of the austenite as well as the martensite. This is indeed the case for the

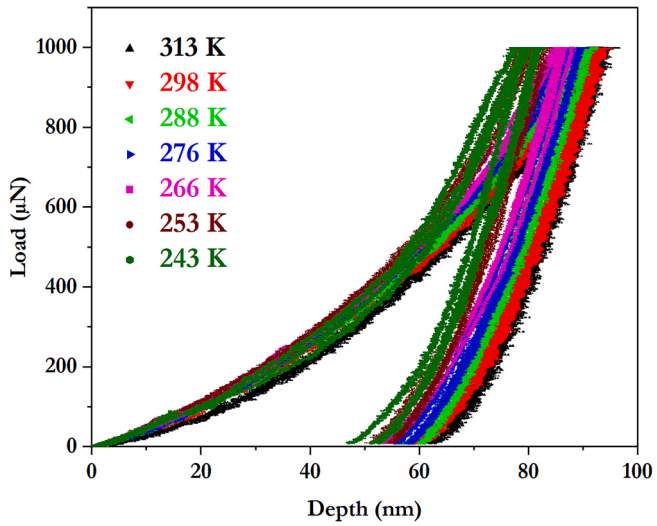

Fig. 6. Temperature-dependent nanoindentation measurements for a 2 μm thick film covering the dual phase austenite and martensite phase regime. No plastic instabilities can be identified across the entire temperature regime.

pop-in behavior at 260 K (Fig. 3), now yielding a CCDF that contains plastic instabilities across a stress range of both the austenite-to-martensite transformation and the twin-variant formation. In other words, both structural mechanisms follow Weibull statistics and can here be distinguished by their corresponding stress scale.

Whilst it is experimentally almost impossible to directly characterize the structural changes during low-temperature indentation, the residual imprint after indentation at room temperature can be assessed with both AFM and TEM to clarify if the pop-in is a signature of dislocation activity or of a phase transformation. The inset in Fig. 2 shows an AFM image of a 298 K-indentation imprint, exhibiting line contrast features that are reminiscent of residual martensite. To gain further insights into possible microstructural changes associated with the pop-in, a TEM analysis of the undeformed thin film and the structure underneath the indents was undertaken. Fig. 5a demonstrates the as-deposited microstructure viewed in bright-field STEM (BF-STEM), for which selected area diffraction (SAD) reveals a pure austenitic phase with a film normal of [001] (Fig. 5b). No pre-existing defect structures or pockets of martensite could be detected along several micrometers of the cross-sectioned thin film.

A different picture emerges when imaging the microstructure underneath an indent location. As can be seen in Fig. 5c, approximately 45°inclined lines appear that have a repeat length scale of around 20 nm and that likely represent martensite variants and remind of the surface topography resolved with AFM. No dislocation structures were identified at indentation locations. SAD from the microstructure underneath the indents reveals the presence of both austenite and an additional phase. In fact, the weaker austenite reflections (*hkl*) = (200), (420), etc.) become too weak to be clearly distinguished and the SAD pattern of the austenite (circles, Fig. 5d) is super positioned with reflections (squares in Fig. 5d) closely located to the austenite peaks positions. These additional reflections suggest the presence of a minor phase which has i) a lattice parameter similar to the austenite phase in the growth direction, ii) a shorter lattice parameter normal to this direction, and iii) a rotation of ~ 6° counterclockwise. For a stoichiometric Ni_2MnGa-alloy or higher Mn-containing systems one would expect the formation of modulated martensite (10 M or 14 M), which consists of a periodic stacking of the tetragonal unit cell disrupted by twin boundaries to minimize the strain energy. These modulated structures distinguish themselves with different crystallography, being a tetragonal unit cell with a > c for 10 M and an orthorhombic unit cell with a > b > c for 14 M. The presence of either 10 M or 14 M martensite would give rise to weak additional diffraction spots along the ⟨110⟩ directions, which however are absent in Fig. 5d. Instead, the SAD pattern in Fig. 5d can be identified as belonging to a non-modulated (NM) martensite, which is in good agreement with Lanska et al. [51] if one extrapolates to the here investigated alloy composition. This NM martensite exhibits a larger

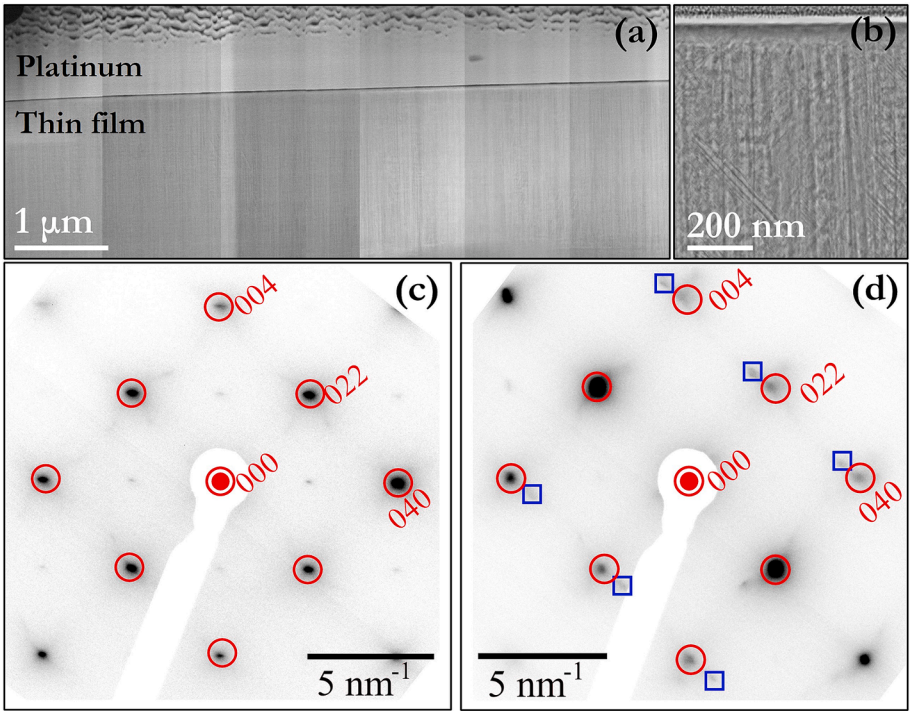

Fig. 7. Bright field STEM overview image of the top part of the 2 μm thick film, including indented regions. No residual indentation structures are present. (b) Zoom-in from (a), highlighting FIB curtaining and isolated defects. These can be found in as-deposited film regions and indented regions. (c) SAD pattern of a defect-free region with B = [100]. (d) SAD pattern of a region containing defects as shown in (b).

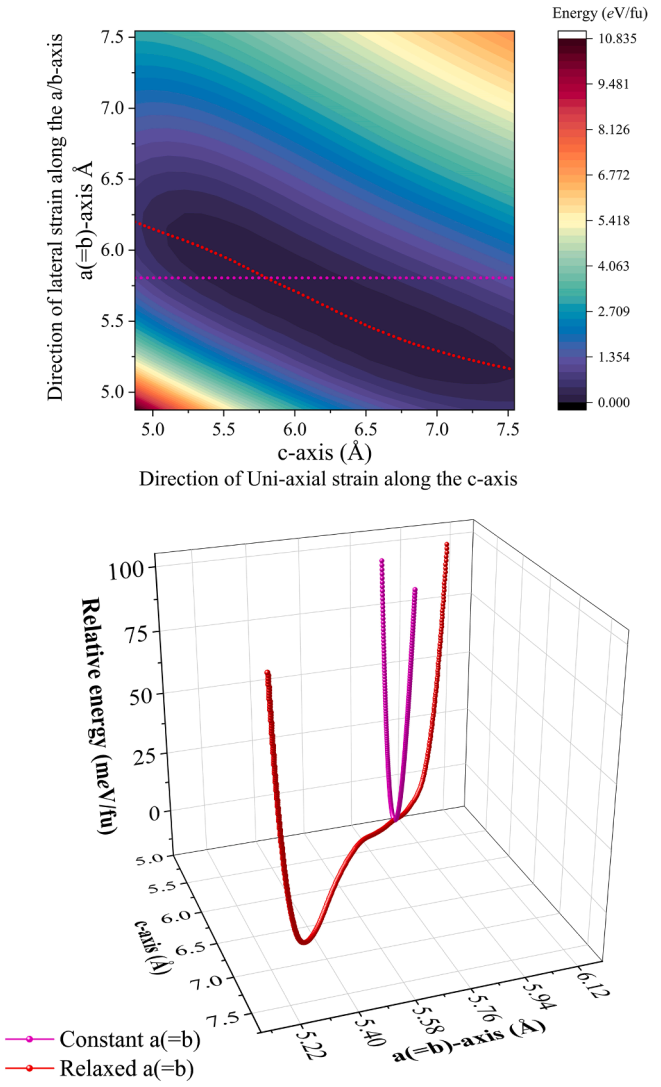

Fig. 8. (a) Ab initio calculation of the potential energy surface (PES) as a function of the lattice constants along the *c*-axis (parallel to the nanoindentation) and the *a*-axis (in the surface plane). (b) Energy profile along the highlighted path where the lattice parameters $a = b$ is allowed to adapt for each indentation depth (red) and where the lattice parameters $a = b$ remain constant (pink).

tetragonal distortion and can thus accommodate a higher strain than modulated martensite [52] at the high triaxial stress state underneath the indenter tip.

3.2. Unconstrained smooth phase transformations

To better understand the formation of the residual NM-martensite underneath the indents in the 0.5 μm thick film, additional temperature dependent nanoindentation experiments were conducted on a 2 μm thick film. Fig. 6 summarizes indentation curves for the temperature range from 243 K to 313 K, where the tests were conducted upon heating from below M_s. Irrespective of temperature, plastic instabilities or pop-ins cannot be identified.

In addition, and in direct comparison to the thinner 0.5 μm film, a significantly softer response is observed. At a displacement of 40 nm upon loading, the thicker film only exhibits a resistance of approximately 200–250 μN (equivalent to a maximum shear stress of 1.83 GPa). The same force or stress level was reached at only 15 nm by the 0.5 μm film. Similarly, the detectable residual depth at unloading is approximately 3 times larger for the thicker film than the 0.5 μm thick film. These differences persist across all temperatures, but the hardest response of the thicker film is expectedly obtained at 243 K, when martensite is probed. The markedly softer mechanical response suggests microstructural phenomena that admit displacement. Since the thin films are free of initial dislocations, any line-defect mediated displacement accumulation can be excluded, leaving austenite-to-martensite driven pseudoelasticity above M_f and twin-boundary motion below M_f as possible mechanisms.

TEM microstructure investigations of the 2 μm film are summarized in Fig. 7. A montage of BF-STEM images of the film including indentation regions is shown in Fig. 7a. Only some vertical streaks due to FIB curtaining can be identified. This is more apparent in higher magnification images, as in Fig. 7b, along with planar defects superficially similar to those in Fig. 5c. SAD patterns from the non-indented regions show only single-phase austenite, with the characteristic alternating weak and strong reflections along the [0 1 0]-type directions (Fig. 7c). In areas containing the planar defects depicted in Fig. 7b, SAD reveals some additional weak spots displaced in the $[\bar{1}10]$-directions relative to the austenite reflections. Such signatures were distributed throughout the film in both non-indented regions and underneath indentation locations, leading to the conclusion that they are not originating from any nanomechanical testing. This, plus the observation that the curtaining lines were deflected by these defects, lead to the conclusion that they are spurious features formed in the thick films during or after lamella preparation.

Despite the clear FIB-introduced curtaining, there is thus no evidence of any dislocations or other phase than austenite in the thick film both in non-indented regions and underneath the indents. That means, all displacement accumulated throughout the curves in Fig. 6 is reversible within the resolution of the experiment. This must further mean that the afore mentioned case of the 0.5 μm film may exhibit the particular incipient pop-in response and formation of NM martensite due to a size and/or constraint effect.

3.3. Ab-initio calculation of stoichiometric Ni_2MnGa

Investigating this further, we resort to ab-initio calculations that were introduced in Section 2. Of particular interest is the change in phase-transformation behavior upon the introduction of lateral constraints, as manifested in the 0.5 μm film. Fig. 8a provides quite generally for the stoichiometric material Ni_2MnGa and various c/a values the potential energy for a range of different $a = b$ values. Under rather unconstrained conditions, transformation-energy minimization corresponds to the red dashed line, whereas the scenario of constant in-plane lattice constants is given by the pink dashed line. For clarity, the energy profiles along the two highlighted lines are additionally provided in Fig. 8b.

In other words, the results of the 0.5 μm film are best described by the scenario of constant in-plane lattice parameters $a = b$. As highlighted by the pink line in Fig. 8b, this scenario only yields a single minimum, without the chance of a martensitic transformation. This means that a coherency constraint to the substrate will enforce that the material remains austenitic for small indentations. Only above a much higher activation stress than for the unconstrained case, the elastic energy will overcome the coherency condition, resulting in a shift into the global minimum at the PES and the pop-in event in the nanoindenter. In contrast, if we assume that the 2 μm thick film corresponds to the scenario of fully adapted lattice parameters $a = b$ (red line in Fig. 8b). We observe in this case a smooth energy profile connecting the austenite and the martensite. Hence, the system can easily undergo the martensitic transformation, once exposed to the mechanical load of the nanoindenter. As such, the computational insights qualitatively support the conclusion that a significantly higher transformation stress is needed under constrained conditions, which manifests itself in the experiments

as a pop-in signature at a stress level between approximately 1.4 and 2.6 GPa, being substantially higher than the few hundred MPa otherwise expected for the phase transformation of bulk crystals [52,53]. We note that such a dramatic increase of the transformation stress is not captured by the Clausius-Claperyon equation, which otherwise can describe temperature-dependent variations of the transformation stress for alloys with different M_s-temperatures.

4. Summary

In anticipation of future small-scale actuation applications of Ni-Mn-Ga shape memory alloys, we have nanomechanically probed the incipient elastic-to-plastic transition of room-temperature austenitic thin films. At a film thickness of 0.5 μm, clear deviations from purely elastic behavior emerge as pop-ins at a stress scale about an order of magnitude larger than for the bulk counterpart. These pop-ins follow Weibull statistics with a shape and scale parameter that is rate and temperature insensitive. Transmission electron microscopy demonstrates that the observed pop-ins originate from an austenite–martensite phase transformation, leaving behind residual martensite underneath indentation sites that based on recent results, can likely be transformed back via thermal cycling [27]. At a larger film thickness of 2 μm, no such nanomechanical instability is observed upon loading and the microstructure underneath indents remains fully austenitic after unloading. Suggesting a strong constraint effect on the phase-transformation behavior, ab-initio calculations were performed. These demonstrate a significant potential energy increase for the martensitic phase transformation when in-plane lattice parameters are constrained and give therefore a rationale for the thickness-dependent incipient phase transformation. Our findings highlight how dimensional constraints may significantly increase the austenite–martensite transformation stress and therefore actuation behavior of Ni-Mn-Ga shape-memory alloys.

Declaration of Competing Interest

The authors declare that they have no known competing financial interests or personal relationships that could have appeared to influence the work reported in this paper.

Data availability

Data will be made available on request.

Acknowledgements

A.F. thanks M. Griepentrog, BAM, for support and training of the nanoindentation method as well as Y. Ikeda, BAM, for TEM support. R. M. is grateful for financial support by the BAM-IFW (Grant No. MIT1-20-63-IFW) funding scheme and for institutional support from BAM. The authors also gratefully acknowledge Heiko Reith (Leibniz IFW Dresden) for supporting the sample preparation, René Hesse (BAM) for TEM sample preparation, and Dorothee Silbernagl (BAM) for help with the AFM measurements. This research was carried out in part at the electron microcopy center at BAM.

References

[1] T. Duerig, A. Pelton, D. Stockel, An overview of nitinol medical applications, Mat. Sci. Eng. A-Struct. 273 (1999) 149–160.
[2] J. Van Humbeeck, Shape memory alloys: A material and a technology, Adv. Eng. Mater. 3 (11) (2001) 837–850.
[3] M. Niinomi, Recent research and development in titanium alloys for biomedical applications and healthcare goods, Sci. Technol. Adv. Mater. 4 (5) (2016) 445–454.
[4] J. Mohd Jani, M. Leary, A. Subic, M.A. Gibson, A review of shape memory alloy research, applications and opportunities, Materials & Design (1980-2015) 56 (2014) 1078-1113.
[5] M. Chmielus, X.X. Zhang, C. Witherspoon, D.C. Dunand, P. Mullner, Giant magnetic-field-induced strains in polycrystalline Ni-Mn-Ga foams, Nat. Mater. 8 (11) (2009) 863–866.
[6] S.A. Wilson, R.P.J. Jourdain, Q. Zhang, R.A. Dorey, C.R. Bowen, M. Willander, Q. U. Wahab, M. Willander, M.A.H. Safaa, O. Nur, E. Quandt, C. Johansson, E. Pagounis, M. Kohl, J. Matovic, B. Samel, W. van der Wijngaart, E.W.H. Jager, D. Carlsson, Z. Djinovic, M. Wegener, C. Moldovan, R. Iosub, E. Abad, M. Wendlandt, C. Rusu, K. Persson, New materials for micro-scale sensors and actuators An engineering review, Mat. Sci. Eng. R 56 (1–6) (2007) 1–129.
[7] W. Huang, On the selection of shape memory alloys for actuators, Mater. Design 23 (1) (2002) 11–19.
[8] S. Fähler, U.K. Rößler, O. Kastner, J. Eckert, G. Eggeler, H. Emmerich, P. Entel, S. Müller, E. Quandt, K. Albe, Caloric Effects in Ferroic Materials: New Concepts for Cooling, Adv. Eng. Mater. 14 (1–2) (2012) 10–19.
[9] T. Gottschall, A. Gracia-Condal, M. Fries, A. Taubel, L. Pfeuffer, L. Manosa, A. Planes, K.P. Skokov, O. Gutfleisch, A multicaloric cooling cycle that exploits thermal hysteresis, Nat. Mater. 17 (10) (2018) 929–934.
[10] P. Hua, K.J. Chu, F.Z. Ren, Q.P. Sun, Cyclic phase transformation behavior of nanocrystalline NiTi at microscale, Acta Mater. 185 (2020) 507–517.
[11] W.J. Buehler, J.V. Gilfrich, R.C. Wiley, Effect of Low-Temperature Phase Changes on the Mechanical Properties of Alloys near Composition TiNi, J. Appl. Phys. 34(5) (1963) 1475-1477.
[12] J.F. Gomez-Cortes, M.L. No, I. Lopez-Ferreno, J. Hernandez-Saz, S.I. Molina, A. Chuvilin, J.M. San Juan, Size effect and scaling power-law for superelasticity in shape-memory alloys at the nanoscale, Nat. Nanotechnol. 12 (8) (2017) 790–796.
[13] V. Fuster, J.F. Gómez-Cortés, M.L. Nó, J.M. San Juan, Universal Scaling Law for the Size Effect on Superelasticity at the Nanoscale Promotes the Use of Shape-Memory Alloys in Stretchable Devices, Adv. Electron. Mater. 6 (2) (2019) 1900741.
[14] K. Ullakko, J.K. Huang, C. Kantner, R.C. OHandley, V.V. Kokorin, Large magnetic-field-induced strains in Ni2MnGa single crystals, Appl. Phys. Lett. 69(13) (1996) 1966-1968.
[15] S.J. Murray, M. Marioni, S.M. Allen, R.C. O'Handley, T.A. Lograsso, 6% magnetic-field-induced strain by twin-boundary motion in ferromagnetic Ni–Mn–Ga, Appl. Phys. Lett. 77 (6) (2000) 886–888.
[16] A. Sozinov, A.A. Likhachev, N. Lanska, K. Ullakko, Giant magnetic-field-induced strain in NiMnGa seven-layered martensitic phase, Appl. Phys. Lett. 80(10) (2002) 1746-1748.
[17] L. Zhou, M.M. Schneider, A. Giri, K. Cho, Y. Sohn, Microstructural and crystallographic characteristics of modulated martensite, non-modulated martensite, and pre-martensitic tweed austenite in Ni-Mn-Ga alloys, Acta Mater. 134 (2017) 93–103.
[18] A. Sozinov, N. Lanska, A. Soroka, W. Zou, 12% magnetic field-induced strain in Ni-Mn-Ga-based non-modulated martensite, Appl. Phys. Lett. 102(2) (2013) 021902.
[19] S. Schwabe, R. Niemann, A. Backen, D. Wolf, C. Damm, T. Walter, H. Seiner, O. Heczko, K. Nielsch, S. Fähler, Building Hierarchical Martensite, Adv. Funct. Mater. 31 (7) (2020) 1–11.
[20] S. Kaufmann, U.K. Rossler, O. Heczko, M. Wuttig, J. Buschbeck, L. Schultz, S. Fahler, Adaptive modulations of martensites, Phys. Rev. Lett. 104 (14) (2010), 145702.
[21] V.A. Chernenko, J. Pons, C. Seguí, E. Cesari, Premartensitic phenomena and other phase transformations in Ni–Mn–Ga alloys studied by dynamical mechanical analysis and electron diffraction, Acta Mater. 50 (1) (2002) 53–60.
[22] S. Kar, Y. Ikeda, K. Lünser, T.G. Woodcock, K. Nielsch, H. Reith, R. Maass, S. Fähler, Growth Twins and Premartensite Microstructure in Epitaxial Ni-Mn-Ga Films, Acta Mater. 252 (2023), 118902.
[23] R. Maaß, P.M. Derlet, Micro-plasticity and recent insights from intermittent and small-scale plasticity, Acta Mater. 143 (2018) 338–363.
[24] G. Laplanche, J. Pfetzing-Micklich, G. Eggeler, Sudden stress-induced transformation events during nanoindentation of NiTi shape memory alloys, Acta Mater. 78 (2014) 144–160.
[25] D.K. Satapathy, S. Aich, Time dependent nanomechanical properties of NiMnGa Heusler alloy, J. Alloy. Compd. 788 (2019) 10–20.
[26] R. Niemann, S. Hahn, A. Diestel, A. Backen, L. Schultz, K. Nielsch, M.F.X. Wagner, S. Fahler, Reducing the nucleation barrier in magnetocaloric Heusler alloys by nanoindentation, Appl. Mater. 4(6) (2016) 1-7.
[27] M. Takhsha Ghahfarokhi, F. Casoli, C. Minnert, S. Bruns, E. Bruder, R. Cabassi, K. Durst, O. Gutfleisch, F. Albertini, Effects of nanoindents on the martensitic transformation of Ni-Mn-Ga shape-memory Heusler films: A study by high-resolution imaging as a function of temperature, Acta Mater. 245 (2023), 118603.
[28] F. Bruederlin, L. Bumke, C. Chluba, H. Ossmer, E. Quandt, M. Kohl, Elastocaloric cooling on the miniature scale: a review on materials and device engineering, Energ. Technol. 6 (8) (2018) 1588–1604.
[29] M. Thomas, O. Heczko, J. Buschbeck, U.K. Rossler, J. McCord, N. Scheerbaum, L. Schultz, S. Fahler, Magnetically induced reorientation of martensite variants in constrained epitaxial Ni-Mn-Ga films grown on MgO(001), New J. Phys. 10 (2) (2008), 023040.
[30] G. Kresse, J. Hafner, Ab initio molecular dynamics for liquid metals, Phys. Rev. B Condens. Matter 47 (1) (1993) 558–561.
[31] G. Kresse, J. Hafner, Ab initio molecular-dynamics simulation of the liquid-metal-amorphous-semiconductor transition in germanium, Phys. Rev. B Condens. Matter 49 (20) (1994) 14251–14269.
[32] G. Kresse, J. Furthmuller, Efficiency of ab-initio total energy calculations for metals and semiconductors using a plane-wave basis set, Comp. Mater. Sci. 6 (1) (1996) 15–50.

[33] G. Kresse, J. Furthmuller, Efficient iterative schemes for ab initio total-energy calculations using a plane-wave basis set, Phys. Rev. B Condens. Matter 54 (16) (1996) 11169–11186.
[34] P.E. Blochl, Projector augmented-wave method, Phys. Rev. B Condens. Matter 50 (24) (1994) 17953–17979.
[35] G. Kresse, D. Joubert, From ultrasoft pseudopotentials to the projector augmented-wave method, Phys. Rev. B Condens. Matter 59 (3) (1999) 1758–1775.
[36] J.P. Perdew, K. Burke, M. Ernzerhof, Generalized gradient approximation made simple, Phys. Rev. Lett. 77 (18) (1996) 3865–3868.
[37] M.A. Uijttewaal, T. Hickel, J. Neugebauer, M.E. Gruner, P. Entel, Understanding the phase transitions of the Ni2MnGa magnetic shape memory system from first principles, Phys. Rev. Lett. 102 (3) (2009), 035702.
[38] B. Dutta, I. Opahle, T. Hickel, Interface effects on the magnetic properties of layered Ni2MnGa/Ni2MnSn alloys: A first-principles investigation, Funct. Mater. Lett. 09 (06) (2017) 1642010.
[39] K.L. Johnson, Contact Mechanics, Cambridge University Press: Cambridge, UK (1985) 84–106.
[40] J. Shimanek, Q. Rizzardi, G. Sparks, P.M. Derlet, R. Maass, Scale-dependent pop-ins in nanoindentation and scale-free plastic fluctuations in microcompression, J. Mater. Res. 35 (2) (2020) 196–205.
[41] J.R. Morris, H. Bei, G.M. Pharr, E.P. George, Size effects and stochastic behavior of nanoindentation pop in, Phys. Rev. Lett. 106 (16) (2011), 165502.
[42] Y. Sato, S. Shinzato, T. Ohmura, T. Hatano, S. Ogata, Unique universal scaling in nanoindentation pop-ins, Nat. Commun. 11 (1) (2020) 4177.
[43] S.G. Corcoran, R.J. Colton, E.T. Lilleodden, W.W. Gerberich, Anomalous plastic deformation at surfaces: Nanoindentation of gold single crystals, Phys. Rev. B 55 (24) (1997) 16057–16060.
[44] C.A. Schuh, A.S. Argon, T.G. Nieh, J. Wadsworth, The transition from localized to homogeneous plasticity during nanoindentation of an amorphous metal, Phil. Mag. 83 (22) (2003) 2585–2597.
[45] B. Gan, S. Tin, Phenomenological description and temperature dependence of serrated flow in Ni-10Pd during high temperature instrumented microindentation, Mat. Sci. Eng. A-Struct. 554 (2012) 41–47.
[46] Y. Ikeda, J. Mancias, B. Gan, R. Maass, Evidence of room-temperature shear-deformation in a Cu-Al intermetallic, Scr. Mater. 190 (2021) 126–130.
[47] C.E. Packard, C.A. Schuh, Initiation of shear bands near a stress concentration in metallic glass, Acta Mater. 55 (16) (2007) 5348–5358.
[48] J. Alstott, E.d. Bullmore, D. Plenz, F. Rapallo, Powerlaw: a Python package for analysis of heavy-tailed distributions, PLoS One 9 (1) (2014) e85777.
[49] P.M. Derlet, R. Maass, The stress statistics of the first pop-in or discrete plastic event in crystal plasticity, Journal of Applied Physics 120(22) (2016) 225101.
[50] R. Niemann, A. Backen, S. Kauffmann-Weiss, C. Behler, U.K. Rossler, H. Seiner, O. Heczko, K. Nielsch, L. Schultz, S. Fahler, Nucleation and growth of hierarchical martensite in epitaxial shape memory films, Acta Mater. 132 (2017) 327–334.
[51] N. Lanska, O. Söderberg, A. Sozinov, Y. Ge, K. Ullakko, V.K. Lindroos, Composition and temperature dependence of the crystal structure of Ni–Mn–Ga alloys, J. Appl. Phys. 95(12) (2004) 8074-8078.
[52] V.A. Chernenko, J. Pons, E. Cesari, K. Ishikawa, Stress-temperature phase diagram of a ferromagnetic Ni-Mn-Ga shape memory alloy, Acta Mater. 53 (19) (2005) 5071–5077.
[53] V.V. Martynov, V.V. Kokorin, The Crystal-Structure of Thermally-Induced and Stress-Induced Martensites in Ni2mnga Single-Crystals, J. Phys. III 2 (5) (1992) 739–749.